Parametric modeling of edge effects for polishing tool influence functions

**Dae Wook Kim,[1*] Won Hyun Park,[1,2] Sug-Whan Kim[2]
and James H. Burge[1]**

[1]*College of Optical Sciences, University of Arizona, 1630 E. University Blvd, Tucson, Arizona 85721, USA*
[2]*Space Optics Laboratory, Dept. of Astronomy, Yonsei University, 134 Sinchon-dong, Seodaemun-gu,
Seoul 120-749, Republic of Korea*
[*]*Corresponding author: letter2dwk@hotmail.com*

Abstract: Computer controlled polishing requires accurate knowledge of the tool influence function (TIF) for the polishing tool (i.e. lap). While a linear Preston's model for material removal allows the TIF to be determined for most cases, nonlinear removal behavior as the tool runs over the edge of the part introduces a difficulty in modeling the edge TIF. We provide a new parametric model that fits 5 parameters to measured data to accurately predict the edge TIF for cases of a polishing tool that is either spinning or orbiting over the edge of the workpiece.

OCIS codes: (220.0220) Optics design and fabrication; (220.4610) Optics fabrication; (220.5450) Polishing

References and links

1. M. Johns, "The Giant Magellan Telescope (GMT)," Proc. SPIE **6986**, 698603 (2008).
2. M. Clampin, "Status of the James Webb Space Telescope (JWST)," Proc. SPIE **7010**, 70100L (2008).
3. R. Aspden, R. McDonough, and F. R. Nitchie, Jr, "Computer assisted optical surfacing," Appl. Opt. **11**, 2739-2747 (1972).
4. R. E. Wagner and R. R. Shannon, "Fabrication of aspherics using a mathematical model for material removal," Appl. Opt. **13**, 1683-1689 (1974).
5. D. J. Bajuk, "Computer controlled generation of rotationally symmetric aspheric surfaces," Opt. Eng. **15**, 401-406 (1976).
6. R. A. Jones, "Grinding and polishing with small tools under computer control," Opt. Eng. **18**, 390-393 (1979).
7. R. A. Jones, "Computer-controlled polishing of telescope mirror segments," Opt. Eng. **22**, 236-240 (1983).
8. R. A. Jones, "Computer-controlled optical surfacing with orbital tool motion," Opt. Eng. **25**, 785-790 (1986).
9. J. R. Johnson and E. Waluschka, "Optical fabrication-process modeling-analysis tool box," Proc. SPIE **1333**, 106-117 (1990).
10. R. A. Jones and W. J. Rupp, "Rapid optical fabrication with CCOS," Proc. SPIE **1333**, 34-43 (1990).
11. D. W. Kim and S. W. Kim, "Static tool influence function for fabrication simulation of hexagonal mirror segments for extremely large telescopes," Opt. Express. **13**, 910-917 (2005).
12. D. D. Walker, A. T. Beaucamp, D. Brooks, V. Doubrovski, M. Cassie, C. Dunn, R. Freeman, A. King, M. Libert, G. McCavana, R. Morton, D. Riley, and J. Simms, "New results from the Precessions polishing process scaled to larger sizes," Proc. SPIE **5494**, 71-80 (2004).
13. E. Luna-Aguilar, A. Cordero-Davila, J. Gonzalez Garcia, M. Nunez-Alfonso, V. H. Cabrera-Pelaez, C. Robledo-Sanchez, J. Cuautle-Cortez, and M. H. Pedrayes-Lopez, "Edge effects with Preston equation," Proc. SPIE **4840**, 598-603 (2003).
14. A. Cordero-Davila, J. Gonzalez-Garcia, M. Pedrayes-Lopez, L. A. Aguilar-Chiu, J. Cuautle-Cortes, and C. Robledo-Sanchez, "Edge effects with the Preston equation for a circular tool and workpiece," Appl. Opt. **43**, 1250-1254 (2004).
15. B. C. Crawford, D. Loomis, N. Schenck, and B. Anderson, Optical Engineering and Fabrication Facility, University of Arizona, 1630 E. University Blvd, Tucson, Arizona 85721, (personal communication, 2008).
16. D. W. Kim, College of Optical Sciences, University of Arizona, 1630 E. University Blvd, Tucson, Arizona 85721, W. H. Park, and J. H. Burge are preparing a manuscript to be called "Edge tool influence function model including tool stiffness and bending effects."

17. D. W. Kim, College of Optical Sciences, University of Arizona, 1630 E. University Blvd, Tucson, Arizona 85721, and J. H. Burge are preparing a manuscript to be called "Time scale dependent conformable tool."

1. Introduction

The demand for an efficient workpiece edge figuring process have been increased due to the popularity of segmented optics in many next generation optical systems, such as the Giant Magellan Telescope (GMT) [1] and James Webb Space Telescope (JWST) [2]. Because those systems have multiple mirror segments as their primary or secondary mirrors, i) the total length of edges is much larger than the conventional system with one mirror; ii) the edges are distributed across the whole pupil. Thus, a precise and efficient edge fabrication method is important to ensure the final performance of the optical system (e.g. light collecting power and spatial resolution based on the point spread function) and reasonable delivery time.

Many Computer Controlled Optical Surfacing (CCOS) techniques have been presented and developed since 1972 [3-10]. The CCOS with its superb ability to control material removal is known as an ideal method to fabricate state-of-the-art optical surfaces, such as meter-class optics, segmented mirrors, off-axis mirrors, and so forth [7-9, 11].

The dwell time map of a tool on the workpiece is usually the primary control parameter to achieve a target removal (i.e. form error on the workpiece) as it can be modulated via altering the transverse speed of the tool on the workpiece [3-10, 12]. In order to calculate an optimized dwell time map, the CCOS mainly relies on a de-convolution process of the target removal using a Tool Influence Function (TIF) (i.e. the material removal map for a given tool and workpiece motion). Thus, one of the most important elements for a successful CCOS is to obtain an accurate TIF.

The TIF can be calculated based on the equation of material removal, Δz, which is known as the Preston's equation [11],

$$\Delta z(x, y) = \kappa \cdot P(x, y) \cdot V_T(x, y) \cdot \Delta t(x, y) \tag{1}$$

where Δz is the integrated material removal from the workpiece surface, κ the Preston coefficient (i.e. removal rate), P pressure on the tool-workpiece contact position, V_T magnitude of relative speed between the tool and workpiece surface and Δt dwell time. It assumes that the integrated material removal, Δz, depends on P, V_T and Δt linearly.

It is well known that a nominal TIF calculated by integrating Eq. (1) under a moving tool fits well to experimental (i.e. measured) TIF as long as the tool stays inside the workpiece [11]. However, once the tool overhangs the edge of workpiece, the measured TIF tends to deviate from the nominal behavior due to dramatically varying pressure range, tool bending, and non-linear effects due to tool material (e.g. pitch) flow [15].

Assuming the linearity of Preston's equation the edge effects can be associated with the pressure distribution on the tool-workpiece contact area. R. A. Jones suggested a linear pressure distribution model in 1986 [8]. Luna-Aguilar, et al.(2003) and Cordero-Davila, et al.(2004) developed this approach further using a non-linear high pressure distribution near the edge-side of the workpiece, however they did not report the model's validity by demonstrating it using experimental evidence [13, 14]. These analytical pressure distributions were fed into the Preston's equation, Eq. (1), to calculate edge TIFs.

For any real polishing tool, the actual removal distribution is a complex function of many factors such as tool-workpiece configuration, tool stiffness, polishing compounds, polishing pad, and so forth. The analytical pressure distribution, $p(x,y)$, approaches [8, 13, 14] tend to ignore some of these effects. Also, in the edge TIF cases, the linearity for Preston's equation may need to be re-considered since the pressure distribution changes in wide pressure value range. The linearity is usually valid for a moderate range of pressure, P, values for a given polishing configuration [15].

Rather than assigning the edge effects to a certain type of analytical pressure distribution model, we define a parametric model based on measured data that allows us to create an accurate TIF without the need of identifying the actual cause of the abnormal behavior in edge removal. We then re-defined the Preston coefficient, κ, which has been regarded as a universal constant in the spatial domain as a function of position in the TIF via the parametric approach. By doing so, we can simulate the combined net effect of many complex factors without adding more terms to the original Preston's equation, Eq. (1).

This paper describes the parametric model and provides examples of its application. Section 2 deals with the theoretical background supporting the parametric edge TIF model. We introduce a functional form of the κ map, and show simulated parametric edge TIFs from the model in Section 3. The experimental demonstration and value of the parametric edge TIF model are summarized in Sections 4 and 5, respectively.

2. Theoretical background for the parametric edge TIF model

2.1 Linear pressure distribution model

Assuming the linear pressure distribution and Preston's relation, we determine the resulting TIF analytically. Assume local coordinate system, (x, y), centered at the workpiece edge with the x axis in the overhang direction (i.e. the radial direction from the workpiece center). The pressure distribution under the tool-workpiece contact area should satisfy two conditions [14]. i) The total force, f_0, applied on the tool should be the same as the integral of the pressure distribution, $p(x,y)$, over the tool-workpiece contact area, A. ii) The total sum of the moment on the tool should be zero. It is assumed that the pressure distribution in y direction is constant, and it is symmetric with respect to the x axis. The moment needs to be calculated about the center of mass of the tool, (x', y') [14]. These two conditions are expressed in Eqs. (2) and (3), respectively.

$$\iint_A p(x, y)dxdy = f_0 \tag{2}$$

$$\iint_A (x - x') \cdot p(x - x', y)dxdy = 0 \tag{3}$$

where x' is the x coordinate of the center of mass of the tool.

While we acknowledge the freedom of choosing virtually any form of mathematical function for the analytical expression of pressure distribution, R.A. Jones introduced the linear pressure distribution model, Eq. (4), in 1986 [8] on the tool-workpiece contact area without detailed study of many higher order factors such as tool bending.

$$p(x, y) = c_1 \cdot x + c_2 \tag{4}$$

The pressure distribution, $p(x,y)$, is determined by solving two equations, Eqs. (2) and (3), for two unknown coefficients, c_1 and c_2. Even though this analytical solution yields negative pressures for large overhang cases [14], we can replace it with zero pressure in practice and solve for c_1 and c_2 by iteration. Some examples of the linear pressure distribution, $p(x)$, are plotted in Fig. 1 (left) when a circular tool overhang ratio, S_{tool}, changes from 0 to 0.3. S_{tool} is defined as the ratio of the overhang distance, H, to the tool width in the overhang direction, W_{tool}, in Fig. 1 (left).

This linear pressure model was fed into the Preston's equation, Eq. (1), to generate the basic edge TIF in Section 3.1.
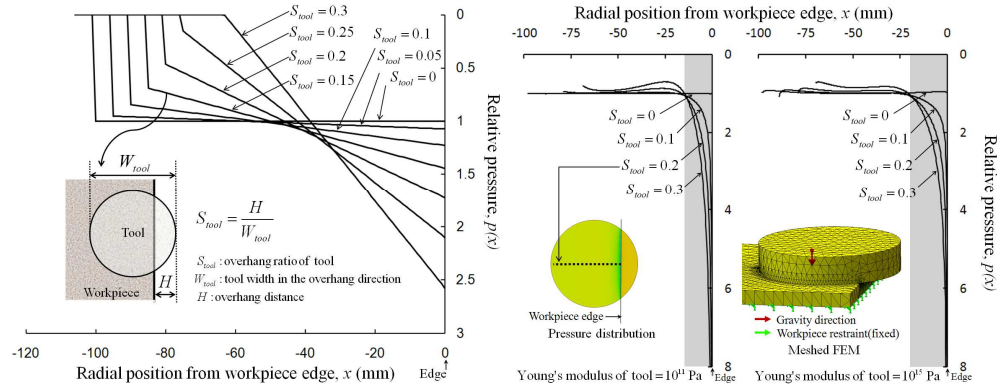
Fig. 1. x-profiles of the pressure distribution, $p(x,y)$, under the tool-workpiece contact area: linear pressure distribution model. (left), static FEA results. (right).

2.2 The first (edge-side) correction

One of the well-known edge removal anomalies is the 'turned-down edge', excessively high removal relative to the target removal near the edge-side [15]. This effect, as shown in the top-right quadrant of Fig. 7 later, cannot be explained by the linear pressure distribution model (i.e. basic edge TIF model). It may result from the non-linear high pressure distribution near the edge-side.

Static Finite Element Analysis (FEA) was performed to characterize a general trend of the edge pressure distribution when tools with different stiffnesses overhang a workpiece. A circular tool and a workpiece were created in a solid model as shown in Fig. 1 (right). For simplicity of the solid model, the effects of the polishing compound between the tool and workpiece were ignored in this study. The polishing compound was assumed as an ideal adhesive, so that the boundary condition at the tool-workpiece interface was set as a 'bonded' case. A next generation edge TIF model based on more comprehensive FEA, that considers the realistic effects of the polishing compound and detailed tool characteristics, will be reported [16]. The Young's modulus of the tool was changed to simulate the effects of the tool stiffness (e.g. 10^{15} Pa: extremely rigid tool and 0.7×10^{11} Pa: typical Aluminum). The tool was deformed by gravity, and the pressure distribution in the gravity direction was calculated under the tool-workpiece contact area.

Two of the FEA results are shown in Fig. 1 (right). There are two major trends in common for most of the FEA results. i) There is a non-linear high pressure distribution in the edge-side, shaded region in Fig. 1 (right). ii) The range of this non-linear distribution remains about same although the overhang ratio, S_{tool}, varies.

The first correction term, f_1, described in detail later in Section 3.2 is formed to correct this edge-side phenomenon.

2.3 The second (workpiece-center-side) correction

Experimentally it was found that the high pressure distribution model used on the edge-side of the tool did not predict the measured behavior at the other side (i.e. workpiece-center-side) of the tool. For an example, more removal than the predicted removal based on the basic edge TIF was observed in the workpiece-center-side of the experimental edge removal profile as shown in the top-right quadrant of Fig. 7. This phenomenon cannot be explained using models which focus only on the edge-side effects. Therefore, we define a second correction term, f_2, to address this discrepancy in Section 3.2. It allows us to increase or decrease the workpiece-center-side removal without considering many factors, such as tool bending effect, non-linearity of the Preston's equation, fluid dynamics of the polishing compound, etc.

3. Parametric edge TIF model

3.1 Generation of the basic edge TIF

For a given tool motion and pressure distribution under the tool-workpiece contact area, a TIF can be calculated using Eq. (1) [11]. The basic edge TIF uses the linear pressure model. Two types of tool motion, orbital and spin, were used in this paper. i) Orbital: The tool orbits around the TIF center with orbital radius, $R_{orbital}$, and does not rotate. ii) Spin: The tool rotates about the center of the tool. These tool motions are depicted in Fig. 2.

The tool overhang ratio, S_{tool}, is fixed for the spin tool motion case, but varies as a function of tool position (A~F in Fig. 2 (left)) for the orbital case while the basic edge TIF calculation is being made.
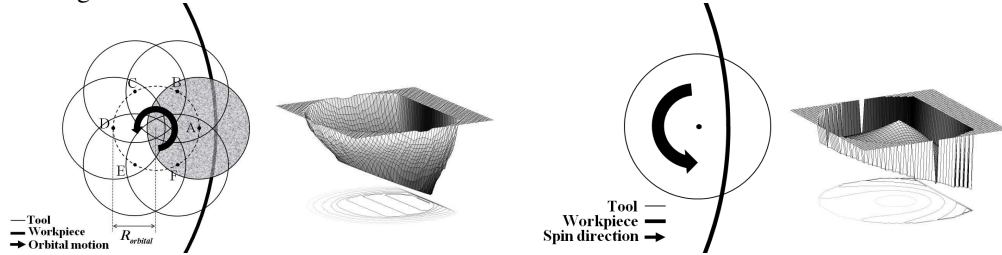
Fig. 2. Orbital (left) and spin (right) tool motion with the basic edge TIF.

3.2 Spatially varying Preston coefficient (κ) map

A new concept using the κ map for the parametric edge TIF model is introduced. The κ map represents the spatial distribution of the Preston coefficient, $\kappa(x,y)$, on the basic edge TIF that already includes the linear pressure gradient. It changes as a function of TIF overhang ratio, S_{TIF}, and five function control parameters (α, β, γ, δ and ε). S_{TIF} is defined as the ratio of the overhang distance, H, to the TIF width in the overhang direction, W_{TIF}, in Fig. 3. The parametric edge TIF can be calculated by multiplying the basic edge TIF by the κ map.
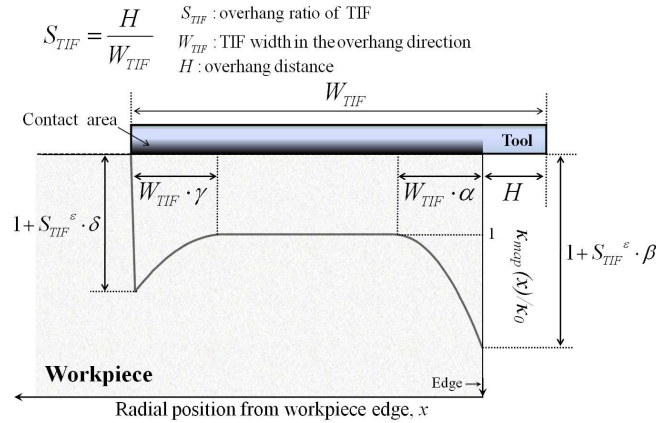

Fig. 3. Degrees of freedom of the κ map (in x-profile) using five parameters.

The TIF width may not be equal to the tool width since it includes the tool motion. For instance, the TIF width is equal to the tool width for the spin motion case. However, for the orbital motion case, the TIF width becomes the sum of the tool width and orbital motion diameter (i.e. $2 \cdot R_{orbital}$).

The virtue of this parametric κ map approach is that it does not require independent understanding of each and every factor affecting the material removal process. Instead, only the combined net effect of them is represented by the κ map. The κ map is defined by a local

coordinate centered at the edge of the workpiece. x represents the radial position from the workpiece edge.

The edge-side high removal, based on the non-linear high pressure distributions near the workpiece edge (mentioned earlier in Section 2.2), is approximated by the first quadratic correction term, f_1, with two parameters, α and β. The first parameter, α, determines the range of the quadratic correction from the edge of the workpiece. The second parameter, β, controls the magnitude of the correction. This degree of freedom using α and β is shown in Fig. 3. This correction is shown graphically in Fig. 3 and defined analytically as

$$f_1(x,\alpha,\beta) = \frac{\beta}{(W_{TIF} \cdot \alpha)^2} \cdot (x + W_{TIF} \cdot \alpha)^2 \cdot \Theta(x + W_{TIF} \cdot \alpha) \tag{5}$$

where $\Theta(z)$ is the step function; 1 for $z \geq 0$ and 0 for $z<0$.

The second correction term, f_2, to address the discrepancy between the simulated (i.e. predicted) edge removal using basic edge TIF and measured edge removal in the workpiece-center-side region (mentioned in Section 2.3) is defined by Eq. (6). Similar to f_1, it has two parameters, γ and δ. The third parameter, γ, determines the range of the second correction, and the fourth parameter, δ, controls the magnitude of the correction as shown in Fig. 3.

$$f_2(x,\gamma,\delta) = \frac{\delta}{(W_{TIF} \cdot \gamma)^2} \cdot (-x - W_{TIF} + W_{TIF} \cdot S_{TIF} + W_{TIF} \cdot \gamma)^2 \cdot \Theta(-x - W_{TIF} + W_{TIF} \cdot S_{TIF} + W_{TIF} \cdot \gamma) \tag{6}$$

The κ map is defined in Eq. (7). It is a sum of the first and second correction terms, and includes a fifth parameter, ε. The fifth parameter, ε, was introduced to change the magnitude of the κ map as a function of TIF overhang ratio, S_{TIF}. Larger ε means that required correction magnitude increases faster as overhang ratio increases.

$$\kappa_{map}(x,\alpha,\beta,\gamma,\delta,\varepsilon) = \kappa_0 \cdot \{1 + S_{TIF}^{\varepsilon} \cdot (f_1 + f_2)\} \tag{7}$$

where the κ_0 is the Preston coefficient when there is no overhang.

The x-profiles of example κ maps are plotted in Fig. 4. An arbitrary parameter set (α=0.2, β=2, γ=0.2, δ=1 and ε=0.2) was used in the example.
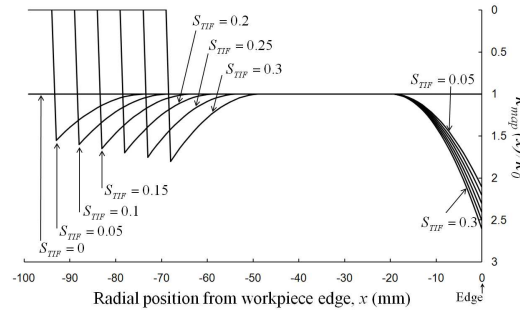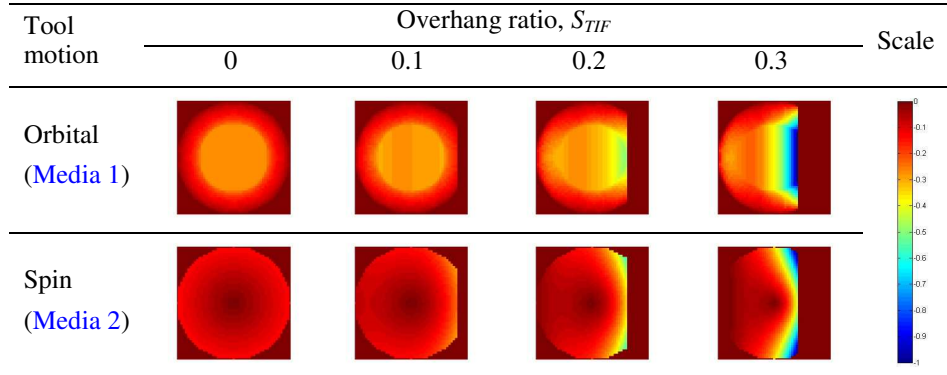

Fig. 4. x-Profiles of κ maps for various overhang ratio, S_{TIF}. (α=0.2, β=2, γ=0.2, δ=1 and ε=0.2).

3.3 Generation of the parametric edge TIF

The parametric edge TIFs for orbital and spin tool motion cases were generated by multiplying the κ map (i.e. the spatial distribution of the Preston's coefficient) by the basic edge TIF (with κ =1) introduced in Section 3.1. The overhang ratio, S_{TIF}, was varied from 0 to 0.3. Five parameter values (α, β, γ, δ, and ε) were used to fit the experimental data in Section 4.1 and 4.2. The parametric edge TIFs are shown in Table 1. As we increase the overhang ratio, S_{TIF}, non-linearly increasing removal near the workpiece edge is clearly shown as a result of the first correctional term for both the orbital and spin cases. The effects of the

second correction are also observed. Due to the opposite signs of δ for the orbital ($\delta = 20$) and spin ($\delta = -3$) cases, in the workpiece-center-side region, there is more and less removal than the basic edge TIF's.

Table 1. Normalized parametric edge TIFs[a]

Tool motion	Overhang ratio, S_{TIF}				Scale
	0	0.1	0.2	0.3	
Orbital (Media 1)					
Spin (Media 2)					

[a](Orbital: α=0.2, β=4, γ=0.4, δ=20, ε=1.5 / Spin: α=0.4, β=6, γ=0.3, δ=-3, ε=0.9)

4. Experimental demonstration of the parametric edge TIF model

Two sets of experiments were used to demonstrate the performance of the parametric edge TIF model. Because the workpiece was rotated in the experiments, integration of parametric edge TIF along the workpiece rotation direction was computed to get the integrated removal profile while considering the workpiece rotation velocity. These model based removal profiles are plotted in Figs. 5 and 6. The conditions for the two edge TIF experiments are provided in Table 2.

Table 2. Edge TIF experiment conditions

Experiment Set No.		1	2
General	Run time	6 hours	1 hour
	Polishing compound	Hastlite ZD	Rhodite
Workpiece	Diameter	660mm	250mm
	Material	ULE	Pyrex
	Surface figure	Convex	Concave
	RPM	6	24
Tool[b]	Polishing Material	Poly-Urethane pad	Poly-Urethane pad
	Diameter	172mm	100mm
	RPM	60 (orbital motion)	30 (spin motion)
	Tool motion	Orbital	Spin
	Orbital radius, $R_{orbital}$	20mm	N/A

[b]More detailed information about the tool will be reported [17].

4.1 Experimental set 1: Orbital tool motion

The first experimental set was performed using orbital tool motion on a ULE workpiece. The overhang ratio was changed for S_{TIF} = 0.05, 0.14, 0.24 and 0.28. The measured removal profiles with RMS error bars are plotted in Fig. 5. The simulated removal profiles based on

the parametric edge TIF model (α=0.2, β=4, γ=0.4, δ=20 and ε=1.5) are also plotted. The five parameters were optimized to fit the experimental data. With one set of parameters, most of the simulated removal profiles for all overhang ratio cases are well fit to the measured removals within the RMS error bars. It means that we can predict all series of removal profiles with any overhang ratio for a given tool and tool motion as long as we perform a few edge runs to determine the tool's characteristic parameter set initially.
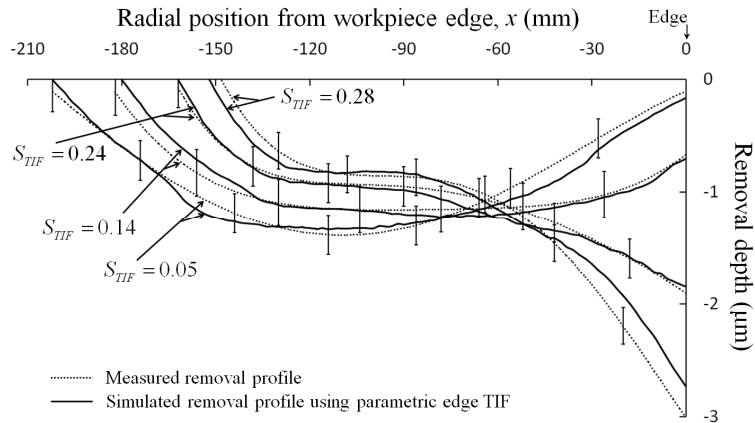
Fig. 5. Measured vs simulated removal profiles: orbital tool motion (α=0.2, β=4, γ=0.4, δ=20, and ε=1.5).

4.2 Experimental set 2: Spin tool motion

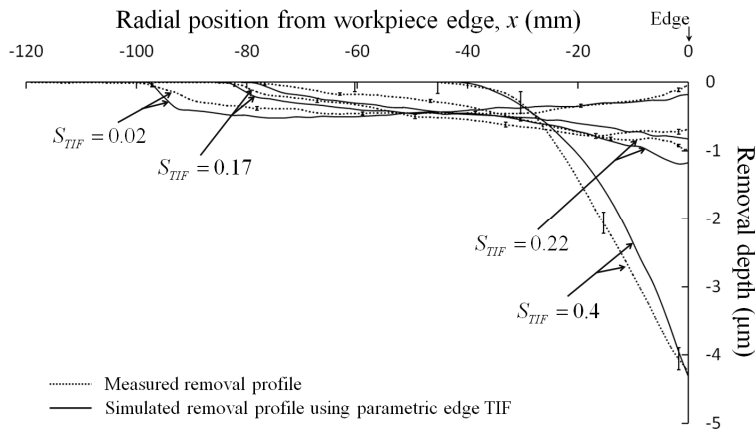The second experimental set was performed using spin tool motion on a Pyrex workpiece.

Fig. 6. Measured vs simulated removal profiles: spin tool motion case (α=0.4, β=6 γ=0.3, δ=-3, and ε=0.9).

The overhang ratio, S_{TIF}, was changed to 0.02, 0.17, 0.22 and 0.4. The measured removal profiles with RMS error bars are plotted in Fig. 6. The simulated removal profiles based on the parametric edge TIF model are plotted also. They are reasonably well matched with the measured removal profiles for all overhang ratio cases including very high overhang ratio case, S_{TIF} = 0.4.

4.3 Performance of the parametric edge TIF model

The comparison between the four different edge TIF models is shown in Fig. 7. The simulated removal profile based on nominal (i.e. no edge model) TIF model does not follow the overall slope of the measured removal profile. Especially, it shows a large difference in the edge-side removal ($x = 0 \sim -60$mm). The computed removal profile using basic edge TIF model seems to have a closer overall slope to the measured removal. However, two mismatches between the measured and simulated removal are clearly observed in the edge-side and workpiece-center-side regions. The parametric edge TIF model using only the first correction allows us to correct the discrepancy in the edge-side removal. The removal profile based on the parametric edge TIF model using both the first and second correction is well matched with the experimental removal profile over the whole range of the removal profile.
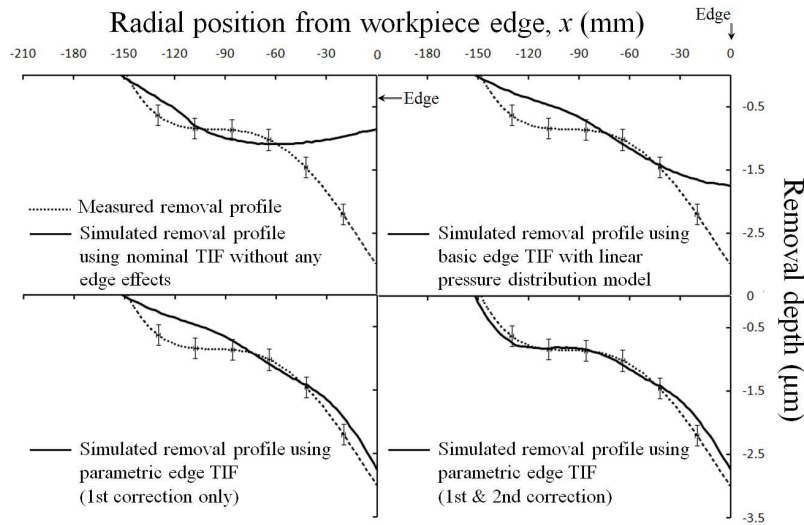

Fig. 7. Measured (with RMS error bars) vs simulated (using different edge TIF models) edge removal profiles for the orbital tool motion case.

The comparison between the four TIF models is presented in Fig. 8. We define normalized fit residual, Δ, as a figure of merit to quantify the performance of the parametric model compared to the data. This is normalized as

$$\Delta = normalized\ fit\ residual = \frac{RMS\ of\ (data - mo\,del)}{RMS\ of\ data} \cdot 100\ (\%) \qquad (8)$$

It is clear that the normalized fit residual, Δ, is relatively low (about 10~20%) for all TIF model cases when the overhang ratio is small ($S_{TIF} < 0.14$ for orbital case and $S_{TIF} < 0.02$ for spin case). It basically means that there is no difference between nominal and edge TIF models when the overhang effects are negligible.

The improvements become significant as the overhang ratio increases. For the orbital tool motion case with $S_{TIF} = 0.28$, the normalized fit residual, Δ, falls to 10% (parametric edge TIF using both corrections) from 52% (nominal TIF), or from 30% (basic edge TIF). For the spin tool motion case with $S_{TIF} = 0.4$, the normalized fit residual, Δ, is dramatically improved to 12% (parametric edge TIF using both corrections) from 87% (nominal TIF), or from 66% (basic edge TIF). The second correction is not really required for the spin tool motion case, in contrast to the orbital tool motion case, where the second correction brought significant improvement.
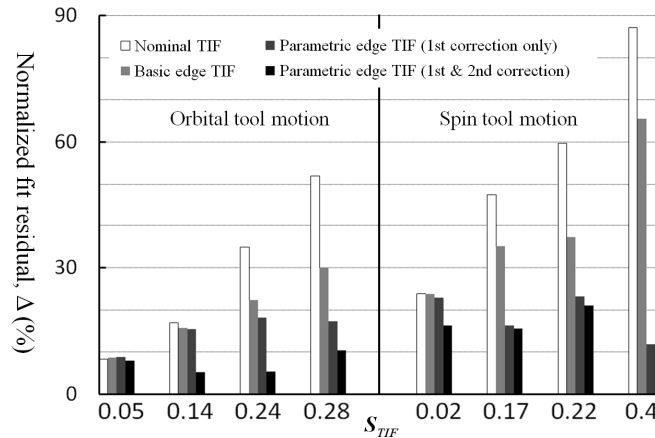
Fig. 8. Normalized fit residual, Δ, of the simulated removal profiles using different TIF models for orbital and spin tool motion cases.

5. Concluding remarks

We presented a parametric edge TIF model that allows accurate simulation of edge effects when a tool overhangs the workpiece edge. Unlike other approaches using analytical pressure distributions to develop edge TIF models, we introduced a parametric approach using a κ map, which represents the spatial distribution of the Preston coefficient. In this way, we were able to express the net effects of many entangled factors affecting the edge removal process in terms of a parametric κ map. Then the parametric edge TIF was derived from a multiplication of the κ map and the basic edge TIF.

Experimental verification for the parametric edge TIF model was successfully performed. The normalized fit residual, Δ, for the simulated removal using the parametric edge TIF model stayed in the 5~20% range for all overhang cases, which allows us to correct about 80% of the surface errors (with an assumption that everything else is ideal) in a single CCOS process. It means that more than 99% of the initial surface errors can be corrected in 3 CCOS runs. Improvement in convergence rate for the residual surface form error is directly related to more efficient time management and lower cost for large optics fabrication projects. Its significance would be even greater for segmented optical system projects, such as GMT [1] and JWST [2], which have more edges across the whole pupil.

Acknowledgments